LETTER https://doi.org/10.53480/bf74-m226

PLANETARY RESEARCH

The SiO_2 abundance on the surfaces of the Moon and Mercury

Christian J. Renggli [1], **Andreas Morlok** [2], **Iris Weber** [2], **Maximilian P. Reitze** [2], **Tommaso Di Rocco** [3], **Jasper Berndt** [4], **Andreas Pack** [3], **Harald Hiesinger** [2]

[1]Max Planck Institute for Solar System Research, Göttingen, Germany
[2]Institut für Planetologie, Universität Münster, Münster, Germany
[3]Geowissenschaftliches Zentrum, Abteilung Geochemie und Isotopengeologie, Universität Göttingen, Germany
[4]Institut für Mineralogie, Universität Münster, Münster, Germany

Corresponding author
(renggli@mps.mpg.de)

Received
January 2, 2026
Accepted
June 3, 2026
Published
August 27, 2026

Handling Editor
Frédéric Schmidt, GEOPS, Université Paris-Saclay, Orsay, France

Article summary

The mid-infrared spectral Christiansen Feature is strongly dependent on a material's SiO_2 content. Here, we present a new calibration of this relationship with an R^2 = 0.957, based on an experimentally extended and methodologically consistent dataset from glasses. The calibration is applied to remote sensing data for the Moon to determine a global SiO_2 surface concentration map.

Abstract

The SiO_2 abundance on rocky planetary surfaces is a key indicator for planetary crust composition and magmatic evolution. The Christiansen Feature (CF) in the mid-infrared provides a mineralogically grounded proxy for the abundance of SiO_2. Here, we present a new experimental calibration based on synthetic glasses with SiO_2 concentrations from 0.5 wt.% to 97.6 wt.% SiO_2. The CF position shows a strong dependence on the SiO_2 concentration, best described by a second-order polynomial (R^2 = 0.957). To test the reliability of the new calibration we apply it to Diviner-derived CF data for the surface of the Moon to produce a global map of SiO_2 on the lunar surface. The results reproduce the mare-highland bimodality and agree well with independent constraints from all lunar sample-return sites. We derive SiO_2 abundances in high-silica regions, including Gruithuisen, Hansteen Alpha, and Lassell Massif with up to 76 wt.% SiO_2. This is the first study that quantitatively derives the high SiO_2 abundances expected in these high-silica regions with an independent compositional calibration. Finally, the new calibration allows the determination of SiO_2 on the surface of Mercury. Using an existing Earth-based CF measurement, we obtain a low abundance of ~37 wt.% SiO_2. High spectral and spatial resolution observations of Mercury by the Mercury Radiometer and Thermal Infrared Spectrometer (MERTIS) on the BepiColombo mission will allow a global application of this new approach, which may be extended to other planetary bodies in the future.

Cite this article as: Renggli, C.J., et al. (2026). The SiO_2 abundance on the surfaces of the Moon and Mercury. *Planetary Research*, **1**(1), 226. https://doi.org/10.53480/bf74-m226

Supplementary material: this article has supplementary material that can be accessed from the online version

Introduction

The SiO_2 concentration in planetary surface materials is a fundamental geochemical indicator used to infer the nature and evolution of planetary crusts. It is a first-order measure of rock composition and the definition of lithologies, correlates with key mineral assemblages, and serves as a proxy for mineralogy and the degree of magmatic differentiation (Salisbury & Walter, 1989). However, the determination of the SiO_2 concentration on the Moon and Mercury by remote sensing observations has proven challenging.

Previously, the Lunar Prospector used gamma-ray spectroscopy to map lunar surface composition and obtained a spatial resolution of 2° per pixel. However, the Lunar Prospector SiO_2 data did not overlap with sample data, showing systematic shifts to lower values (Prettyman et al., 2006). More recently, a machine learning approach based on SELENE multiband imager data and constrained by Chang'e-5 sample compositions was used to generate new compositional maps of the Moon (Yang et al., 2023). Ma et al. (2022, 2023) used Lunar Reconnaissance Orbiter (LRO) Diviner data to determine lunar surface composition maps. A convolutional neural network based on data in the visible and mid-infrared spectral range was used to obtain a lunar SiO_2 map with good agreement with previous gamma-ray observations, but which fails to detect the high-silica regions (Chen et al., 2025). In this study we use a different approach and present a new independently calibrated relationship of SiO_2 abundance and the Christiansen Feature (CF) in the mid-infrared spectral range.

For Mercury, the X-ray spectrometer on the NASA MESSENGER mission constrained the surface composition (Nittler et al., 2011, 2018, 2020). The instrument determined element ratios, which were then used to calculate absolute concentrations of oxides including SiO_2. Similarly, MIXS (Mercury Imaging X-Ray Spectrometer) on the BepiColombo (Benkhoff et al., 2021) mission will primarily provide element ratios for the surface of Mercury (Bunce et al., 2020). In addition, MERTIS (MErcury Radiometer and Thermal Infrared Spectrometer) will map the surface of Mercury in the mid-infrared spectral range of 7 to 14 µm and constrain the surface mineralogy of the planet, including measurement of the CF with high spectral resolution (Hiesinger et al., 2020).

Here, we present a significantly improved calibration of an independent measure for the SiO_2 concentration in planetary silicate surface materials, based on the position of the CF in the mid-infrared spectral range. The CF is defined as the reflectance minimum or emission maximum, and occurs where the refractive index of a material reaches unity. The CF has previously been suggested to linearly depend on the chemical composition of silicates (Conel, 1969; Cooper et al., 2002, Kumari et al., 2025, Pisello et al., 2022, Weber et al., 2023).

Multiple factors influence the CF position, including pressure environment, temperature, irradiation, and grain size, with decreasing pressure and temperature shifting the CF to lower wavelengths, while increased solar irradiation and smaller grain sizes (particularly 0-32 µm fractions) shift it to higher wavelengths (Donaldson Hanna et al., 2017; Logan & Hunt, 1970; Logan et al., 1973; Henderson and Jakosky, 1997; Shirley & Glotch, 2019; Donaldson Hanna et al., 2012). The effect of space weathering on the CF position remains debated (Kumari et al., 2024a), with Salisbury et al. (1997) and Lucey et al. (2017) reporting no significant correlation between the CF position and I_s/FeO, the standard measure for lunar soil maturity defined as the abundance of nanophase iron relative to the bulk FeO content. Furthermore, simulated micrometeorite bombardment in experiments does not lead to a shift in the CF (Weber et al., 2020). Since laboratory analysis of heterogeneous analogue material mixtures involves many parameters often counteracting each other, silicate glasses with broad compositional variations serve as ideal analogues to isolate and calibrate the compositional dependence of the CF position specifically, as no significant CF shifts are observed with varying grain size fractions or between different measurement methods (Morlok et al., 2017; Morlok et al., 2021; Morlok et al., 2022).

Our new approach, therefore, involves an extension of the compositional range to extreme SiO_2 contents, with the synthesis of glasses ranging from 0.5 wt.% to 97.6 wt.% SiO_2. Glasses are ideal analogue materials to study compositional variations on atmosphere-less planetary bodies such as the Moon and Mercury. They are highly abundant on the lunar surface formed by pyroclastic and effusive volcanism, impact processes, and space weathering (Morlok et al., 2021, Wilbur et al., 2025, Zhao et al., 2023).

Our approach allows a reliable compositional mapping for SiO_2 on the surface of the Moon, even based on data with very low spectral resolution provided by the three narrow-band channels of the Diviner instrument on the Lunar Reconnaissance Orbiter (Lucey et al., 2021). With this new calibration, the spectral measurement of the CF by MERTIS on the surface of Mercury will allow the independent quantification of SiO_2 on the planet's surface.

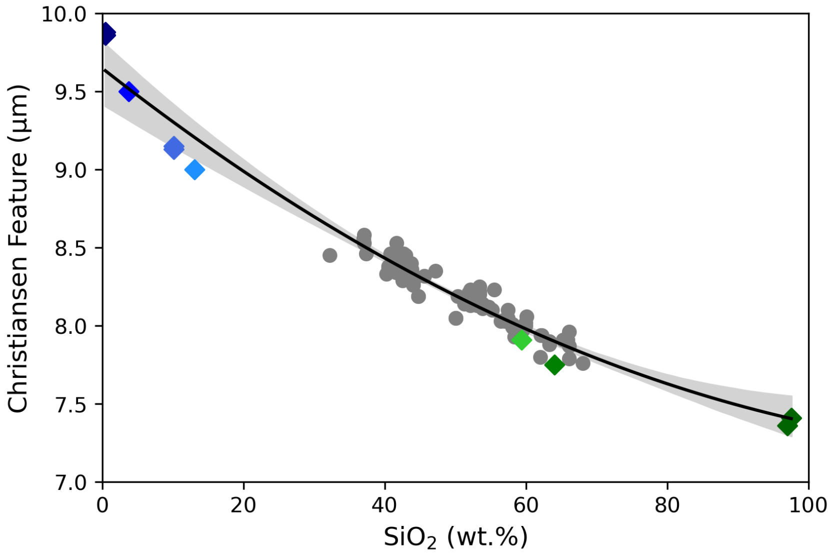

Figure 1 | The CF position in μm as a function of the SiO_2 wt.% concentration in the glasses. Grey circles represent literature data. The black line with a grey error envelope represents the best fit second-order polynomial through all data including our new synthetic glasses and the literature values. Note that we use an internally consistent dataset with only glass samples measured by reflectance micro-FTIR. The R^2 value of the best fit is 0.957.

Results and discussion

Calibration of the Christiansen Feature

The position of the CF shows the best resolved systematic spectral shift as a function of the SiO_2 concentration (Fig. 1). The positions of the CF are listed in Table S1 and increase with decreasing SiO_2 from 7.4 μm at 97.6 wt.% to 9.9 μm at 0.5 wt.% SiO_2. Full FTIR and Raman spectra are shown in the supplementary Figures S2 and S3 (see methods for details). For the calibration we include literature data of *CF* positions measured for planetary analogue glasses, that were measured by micro FTIR specular reflectance on polished surfaces (Haupt et al., 2026; Morlok et al., 2017, 2020, 2021). The data are chosen for pure glasses without crystallization features, with the same spectral resolution. This guarantees identical analytical conditions to avoid features that do not come from the compositional effect, which we calibrate for. The best fit to the data in wt.% of SiO_2 is a 2nd order polynomial:

$$CF = 1.28 \times 10^{-4} \left[SiO_2\right]^2 - 3.55 \times 10^{-2} \left[SiO_2\right] + 9.649$$

with the *CF* wavelength in μm and an R^2 of 0.957 (Table S2). A linear fit, previously used to describe the SiO_2 dependence of *CF* (Cooper et al., 2002) does not sufficiently account for the observations at extremely low or high SiO_2 concentrations in the glasses. Cooper et al. (2002) obtained an R^2 = 0.772 for their dataset, whereas our internally consistent dataset has an R^2 = 0.926 when fitted with a linear function. Finally, the best fit is achieved for the relationship of CF with the molar concentration of SiO_2 in the glasses using a 2nd order polynomial (R^2 = 0.966). From the scatter in our data, we estimate an uncertainty for the calibration of ± 3.4 wt.% SiO_2.

The spectral range of 7 to 14 μm in the mid-infrared is sensitive to the SiO_2 concentration in silicate glasses due to the dependence on Si-O bond vibrations, both in emission and in reflectance spectroscopy (Lee et al., 2010). This is of particular interest for remote sensing observations, where direct in-situ measurements of chemical compositions are not possible or limited, such as the observation of airless planetary bodies, including the surfaces of asteroids, Mercury, or the Moon. Here, we test the new calibration of the SiO_2-CF relationship by applying it to a lunar CF dataset and compare the outcome to compositional data from returned lunar samples.

SiO_2 on the lunar surface

The Diviner spectrometer mapped the surface of the Moon with three narrow-band channels near 8 μm, which allowed the calculation of the CF spectral positions (Donaldson Hanna et al., 2017; Greenhagen et al., 2010; Lucey et al., 2017). Here, we use a global CF dataset for the Moon, which was corrected for illumination, topography, geometry, and space weathering effects by Lucey et al. (2021) as shown in their Figure 8 and openly available at http://doi.org/https://doi.org/10.5281/zenodo.4558194. The map has a resolution of 32 pixels per degree, covering all longitudes and ±70° latitude. Lucey et al. (2021)

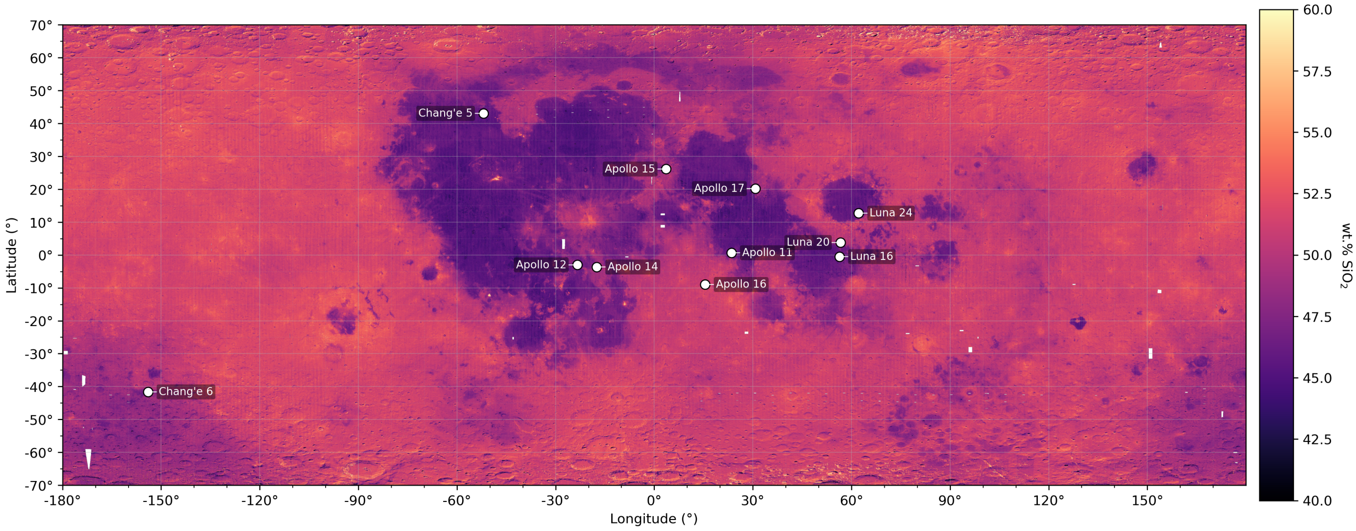

Figure 2 | Calculated SiO_2 wt.% surface abundance on the Moon with the Apollo, Luna, and Chang'e landing sites, from which these missions returned samples.

noted that some artifacts remained at high latitudes (> 50°), which remain notable in the global map of SiO_2 wt.% at > ±50° latitude, calculated using the newly calibrated 2nd order polynomial from Table S2. Lucey et al. (2021) estimate an uncertainty of 0.02 µm for their corrected CF wavelengths. In the compositional range of mare basalts and anorthosites this translates to an uncertainty of 1 wt.% SiO_2.

Comparison with returned samples from lunar missions

The calculated SiO_2 wt.% concentration on the surface of the Moon follows a bimodal distribution (Fig. 2), which is well established due to the presence of lunar highlands and mare basalts. Here, the concentration of SiO_2 quantifies this bimodality with mean mare terrain concentrations of 45.8 ± 0.9 wt.% SiO_2 and the highland regions with 50.9 ± 1.6 wt.% SiO_2. To ground-truth our calibration we take a closer look at the landing sites from which we have returned samles (Apollo, Luna, Chang'e). For each landing site we calculate average SiO_2 concentrations over a circular area with a radius of 0.5°, averaging over ~800 pixels per landing site (Table S3). A comparison of the calculated landing site compositions and the returned samples is shown for the Apollo missions in the supplementary figure S4, and for the Chang'e and Luna samples in S5.

The calculated average mare SiO_2 concentration is best represented by the landing sites of Apollo 11, 12, Luna 16, 24, and Chang'e 5, whereas the highland regions are best represented by the Apollo 16 landing site (Table S3, Figs. S4 & S5). Here, we make a comparison of our calculated regional landing site SiO_2 concentrations and reported data for returned lunar samples from these sites providing ground truth. The average reported soil composition of the Apollo 11 landing site has 42.0 ± 0.3 wt.% SiO_2 (Heiken et al., 1991) and average mare basalt compositions have 41.3 ± 2.5 SiO_2 wt.% (Lunar Sample Compendium, 2012). Returned soil and basalt rock samples have similar SiO_2 concentrations and are ~4 wt.% below those inferred for the Apollo 11 landing site radius based on our calculations (46.2 ± 0.7 wt.%). However, we calculate average compositions over a much larger area of ~70'000 km^2 with a radius of 0.5°. This larger region is likely influenced by higher SiO_2 abundances in the highland terranes south of Mare Tranquilitatis. More than 30% of the SiO_2 in Apollo 11 regolith has elevated SiO_2 abundances, including feldspathic upper crust and KREEP materials. Furthermore, the Apollo 11 landing site is affected by crater rays from Theophilius crater 380 km south-south-east in highland terrane (Korotev & Gillis, 2001).

For Apollo 12, Apollo 14, and Apollo 15 we obtain very good agreements between the calculated SiO_2 concentrations at the landing sites (Table S3, Fig. S4) and average soil compositions with 46.3 wt.% (Apollo 12), 48.1 wt.% (Apollo 14), and 46.8 wt.% (Apollo 15) respectively (Heiken et al., 1991). On the other hand, we obtain a regional SiO_2 concentration at the Apollo 16 site of 51 ± 0.9 wt.%, which is significantly higher than the average soil returned by Apollo 16 at 45 wt.% SiO_2 (Heiken et al., 1991). However, local highland basalts (67559, 67747, 67945) at the Apollo 16 site have elevated SiO_2 contents with an average of 47.2 ± 2.2 wt.% (Lunar Sample Compendium, 2012). The high calculated SiO_2 concentration derived for the Apollo 16 landing site region and the highland regions in general, suggests that previous models may have underestimated the abundance of high-Mg suite lithologies such as norites in these terranes. The Apollo 17 landing site shows the largest compositional diversity in calculated SiO_2 and we determine 48.5 ± 1.5 wt.% (Table S3). This is also reflected by the compositional variability of the returned Apollo 17 samples, with an average soil composition of 43.2 wt.% SiO_2 (Heiken et al., 1991) compared to an average basalt composition of only 38.9 ± 1.2 wt.%, based on samples compiled in the "Lunar Sample Compendium" (2012). However, abundant impact melt breccias have higher SiO_2 contents of 46.6 ± 1.6 wt.%. The returned samples also include norites with 49.4 ± 1.8 wt.%, contributing to the compositional spread and the higher SiO_2 abundance at the landing site, which we determined.

The newly determined SiO_2 abundance at the Luna 16 landing site, with 45.7 ± 0.6 wt.%, is similar to Apollo 11, and falls in the range of compositions reported for Luna 16 fragments, including igneous, microbreccia and lithic fragments (Keil et al., 1972). The Luna 20 landing site region has a SiO_2 concentration of 49.7 ± 0.8 wt.% typical for highland terranes, whereas Luna 24 has 45.6 ± 0.7 wt.% and is representative of average mare terranes and in excellent agreement with average Luna 24 bulk lithologies at 45.7 ± 1.5 wt.% (Taylor et al., 1978). For the Chang'e 5 landing site area we obtain 45.9 ± 0.6 wt.% SiO_2, which is higher than reported soil compositions of 42.2 ± 0.3 wt.% (Li et al., 2022) or 41.3 ± 1.5 wt.% (Zong et al., 2022), but in the range of mare basalt fragments with 41.8 ± 2.3 to 44.5 ± 3.8 wt.% SiO_2 (Boschi et al., 2023; Che et al., 2021) and pyroclastic glasses with 46.8 ± 0.5 wt.% SiO_2 (Wang et al., 2024). Finally, for Chang'e 6 we obtain 47.0 ± 0.7 wt.% SiO_2 (Table S3), in the range of soil compositions reported for the returned samples at 45.6 to 46 wt.% SiO_2 (Li et al., 2024) and significant contributions of non-mare noritic ejecta with 46.9 ± 0.2 wt.% SiO_2 (Wang et al., 2025).

Here, we compare our new calibration and calculated SiO_2 abundances on the Moon with other literature approaches (Fig. S6). First, we applied the linear CF-SiO_2 relationship from Kumari et al. (2025) to the same CF dataset by Lucey et al. (2021) to which we applied our new calibration. This approach yields a narrower bimodal distribution of SiO_2 compared to our calibration, with mare terrain SiO_2 concentrations of 48.3 ± 0.5 wt.% SiO_2 and the highland regions with 50.7 ± 0.7 wt.% SiO_2. The comparison with returned lunar samples shows that the linear CF-SiO_2 relationship from Kumari et al. (2025) results in systematically overestimated SiO_2 abundances for mare terrains in particular (Fig. S6). Second, we compare our calculated SiO_2 abundances to the model by Ma et al. (2025). The histograms show that their calculated SiO_2 concentrations are affected by model artefacts and do not show natural distributions, which fail to reproduce lunar sample compositions and underestimate SiO_2 concentrations (Fig. S6).

The significantly improved reproducibility of compositional ranges at landing sites for which returned samples are available, based on our new calibration, allows us to discuss the SiO_2 abundances in other lunar regions and surface features more reliably. For example, the pyroclastic Orientale ring dark mantle deposit (Weitz et al., 1998) is clearly apparent with lower SiO_2 concentrations relative to the surrounding highlands, south-west of the Orientale basin (Fig 2). We also find calculated SiO_2 abundances in the South Pole-Aitken basin (SPA) that are lower compared to the average highland terranes. This is in contrast to Chen et al. (2025) who find highest SiO_2 concentrations of up to 50 wt.% in the SPA. Notably, their observations for the SPA are also elevated relative to their Chang'e 6 reference. However, our comparison with Chang'e 6 samples suggest a very good agreement with our own model. The SPA is of particular petrological interest due to the thin lunar crust (Wieczorek et al., 2013) and potentially exposed lunar mantle lithologies (Moriarty et al., 2021). Due to the high southern latitude of the SPA the CF dataset is increasingly affected by remaining artefacts (Lucey et al., 2021), which is evident in the apparent topographic features of the SiO_2 map at latitudes > ± 45° (Fig. 2).

SiO_2 in highly silicic terranes

The calculated SiO_2 map reliably highlights highly silicic compositions in the central mare region, which were previously identified based on low wavelength CF (Glotch et al., 2010, Kumari et al., 2024b), shown in Figure 3. Based on the CF positions (Glotch et al., 2010) we obtain 49.7 wt.% SiO_2 for Helmet, 54.7 wt.% for Southern Montes Riphaeus, 60.0 wt.% for Hansteen Alpha, 62.5 wt.% for Gruithuisen Domes (ɣ), 74.2 wt.% for Aristarchus Crater, and 76.0 wt.% for the Lassell Massif. For the first time, we obtain quantitative SiO_2 concentrations for these exceptionally silicic localities. They are generally also depleted in FeO and TiO_2 and rich in Th (Hagerty et al., 2006). The silicic domes have received increased attention in the past years and have been suggested to be analogous features to terrestrial rhyolite domes (Ashley et al., 2016; Boyce et al., 2017; Glotch et al., 2021; Gullikson et al., 2016; Hawke et al., 2003; Qiu et al., 2022, 2023, 2025; Ravi et al., 2025). The highly silicic localities were not yet directly sampled by a mission, but there are examples of SiO_2-rich, even granitic grains and clasts in returned breccias with up to 75 wt.% SiO_2 (Rutherford et al., 1976; Seddio et al., 2013, 2014; Valencia et al., 2024; Warren et al., 1983).

The compositional variability in the samples of a given landing site have shown that a calibration of the SiO_2 abundance on these samples alone, for the extrapolation to the entire lunar surface via spectral observations (Chen et al., 2025; Ma et al., 2022; Yang et al., 2023) is not sufficiently reliable and require an independent calibration of the SiO_2 concentration on the CF position. The present study is the first that reliably quantifies the high-silica regions with compositions expected based on returned lunar granitic

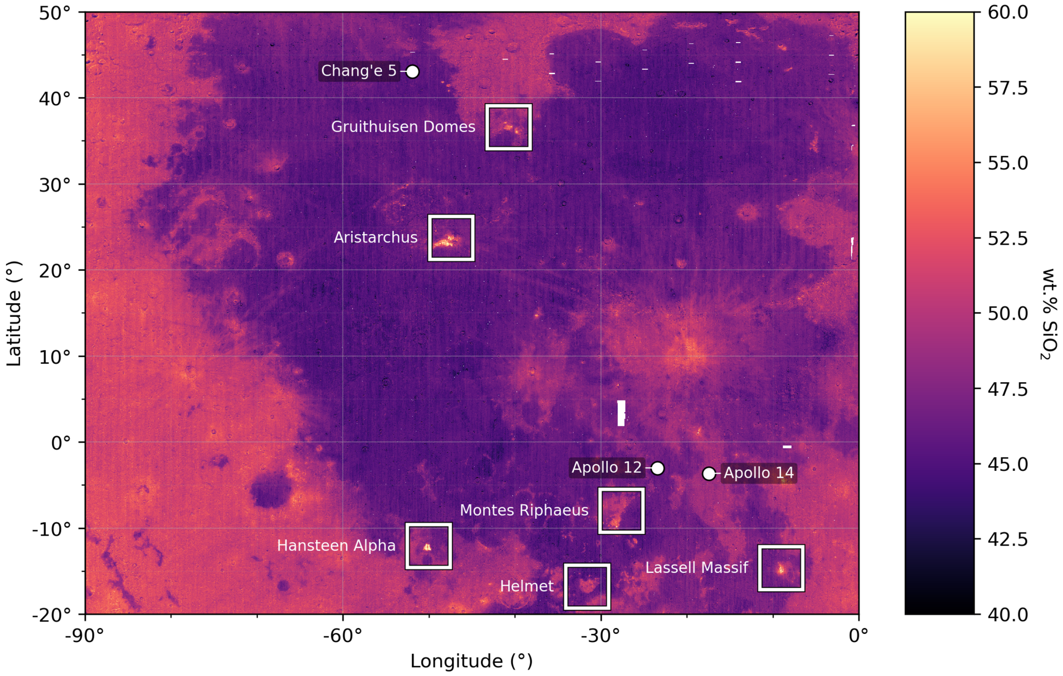

Figure 3 | Calculated SiO_2 concentration map over the central mare region with highly silicic localities identified by Glotch et al. (2010). These silicic domes and craters exhibit SiO_2 concentrations of up to 76 wt.% at Lassell Massif.

breccias, and which is independently validated via the returned samples suites (Figs. S4, S5). For example, the inversion models by Chen et al. (2025) and Ma et al. (2022), both partially based on the CF map from the Diviner mission, fail to reproduce the high SiO_2 abundances at Aristarchus, Gruithuisen Domes, Lassell Massif, and Hansteen. On the other hand, observations by the gamma-ray spectrometer on the Lunar Prospector had insufficient spatial resolution to detect these regions, and also failed to resolve SiO_2 in the South Pole-Aitken basin (Prettyman et al., 2006). Finally, the estimates of the SiO_2 distribution will strongly benefit in the future from CF measurements at high spectral resolution over the spectral range from 7 to 10 µm, and are an important constraint for future landed missions to the Moon, including human exploration and in-situ resource applications (Anand et al., 2012).

Implications for Mercury

The MERTIS instrument on the BepiColombo mission to Mercury provides such a high spectral resolution of up to 90 nm (Hiesinger et al., 2020; Hiesinger & Helbert, 2010). The measurement of SiO_2 on Mercury with the MERTIS instrument relies on our new calibration, since no reference samples are available. We will apply the calibration to global data of Mercury following the start of the science phase of the BepiColombo mission in 2027.

For now, CF data for the surface of Mercury is very limited. However, Earth-based observations provided an estimate for the CF at ~8.5 µm (Sprague, 2000). Based on our model this would equate to 37.4 wt.% SiO_2. This is significantly lower than previous estimates for the SiO_2 concentration on the surface of Mercury in the range of 49 to 60 wt.% SiO_2 (Vander Kaaden et al., 2017). These numbers were calculated from element ratios measured by the X-spectrometer and Si abundance measurements from the gamma-ray spectrometer on the MESSENGER mission (Evans et al., 2012; Nittler et al., 2018; Weider et al., 2015). Given the high uncertainty on the absolute Si abundances measured by gamma-ray spectrometry (24.6 ± 7 %), 25% have been used and oxide concentrations were then calculated based on assumed valence states (Nittler et al., 2011, 2018; Vander Kaaden & McCubbin, 2016; Weider et al., 2012, 2014). However, this approach does not account for the observed low O/Si ratio, which requires some of the Si to be hosted as a metallic or carbide phase (Iacovino et al., 2023; McCubbin et al., 2017). Our determined low SiO_2 abundance is in line with the hypothesis that significant amounts of Si are present in a reduced metallic or carbide phase. The X-ray spectrometer MIXS (Mercury Imaging X-ray Spectrometer) on BepiColombo will produce global chemical maps of Mercury, but these data will also primarily be elemental ratios (Bunce et al., 2020; Fraser et al., 2010; Martindale et al., 2023). Here, the new calibration of the CF will provide an independent quantification of the SiO_2 abundance on Mercury. Finally, the relationship between the CF and SiO_2 abundance will allow direct compositional constraints of terrestrial exoplanets with exposed rocky surfaces, following a recent analysis that suggested the measurement of CFs of exoplanets with the James Webb Space Telescope (First et al., 2025).

Acknowledgements. C.R. is funded by the European Union (ERC, ELMO, 101219152). Views and opinions expressed are however those of the author(s) only and do not necessarily reflect those of the European Union or the European Research Council. Neither the European Union nor the granting authority can be held responsible for them. A.M., I.W., and M.P.R. are supported by DLR grant 50 QW 2201A.

Open science statements

Author contributions

- **Conceptualization**: Renggli, Morlok
- **Data curation**: Weber, Reitze, Morlok
- **Formal analysis**: Renggli, Morlok, Weber
- **Funding acquisition:** Renggli, Hiesinger
- **Investigation:** Renggli, Morlok, Weber, Reitze, Di Rocco, Berndt, Pack
- **Methodology**: Renggli, Morlok, Pack
- **Project administration**: Renggli
- **Validation**: Renggli
- **Visualization:** Renggli
- **Writing - original draft:** Renggli
- **Writing - review and editing**: Morlok, Weber, Reitze, Di Rocco, Pack

Data availability Published infrared spectra and chemical compositions are available along with additional information in the MERTIS IRIS infrared spectral database with the IDs given in Table S1 at http://doi.org/https://iris.uni-muenster.de/. The SiO_2 wt.% map, as well as the FTIR and Raman spectral files, are available on zenodo.org via http://doi.org/https://doi.org/10.5281/zenodo.17940737.
Competing interests The authors declare no competing and financial interests.

Methods

Glasses were synthesized from reagent grade oxides (SiO_2, TiO_2, Al_2O_3, Fe_2O_3, and MgO) and $CaCO_3$, ground and mixed in ethanol. The mixtures were decarbonated at 1000 °C for 6 h in air, and reduced in a 1-atm CO-CO_2 gas-mixing furnace (Gero GmbH, Germany) in the experimental petrology laboratories at the University of Münster in Al_2O_3 crucibles at 1000 °C one logfO_2 unit above the Iron-Wüstite (IW) buffer to ensure that all iron was present as FeO in the mixtures.

The powders were mounted in a Ni holder and placed in vacuum (~6×10^{-7} mbar) for the glass synthesis with a 50 W CO_2 laser focused to < 1 mm^2 on the powder mixtures. The laser system allowed heating above 2000 °C, which was required for the extreme glass compositions (Table S1). The laser was operated at only 7% of its power and targeted at the powders for ~30 s. These parameters were optimized in multiple attempts to obtain sufficient melting of the samples. The obtained beads have diameters in the orders of 500 µm and show variable degrees of quench crystallization (Fig. S1). However, the samples were sufficiently glassy to allow the measurements of the chemical compositions, Raman, and micro-FTIR (Fourier Transform Infrared Spectroscopy) measurements of homogeneous glass areas.

The obtained beads were mounted in epoxy resin and polished to a 1/4 µm finish and imaged with a JEOL JSM-IT510LA Analytical Scanning Electron Microscopy at the Max Planck Institute for Solar System Research (MPS). Back-scattered electron images were obtained to document the samples and test for the presence of quench crystals and homogeneous glassy areas. Here, we present the seven successful samples with sufficient homogeneous glass. Raman spectra were measured with a WITec alpha300 AR Raman microscope (50x objective) equipped with a 532 nm laser at the MPS. Spectra were accumulated for 1 s integration time and 30 repetitions at a laser power of 1 mW.

The chemical compositions of the glasses were measured with a JEOL JXA 8530 F Hyperprobe in wavelength-dispersive mode at the Institute for Mineralogy, University of Münster. Measurements were conducted at an acceleration voltage of 15 kV, a probe current of 10 nA, and a beam diameter of 10 µm, to minimize Na-loss. Both synthetic and natural standards were used for WDS. Hypersthene (Si), rutile (Ti), kyanite (Al), fayalite (Fe), San Carlos olivine (Mg), and diopside (Ca) were used as reference materials.

Mid-infrared reflectance spectra were measured with a dry-purged Hyperion 3000 FTIR microscope coupled to a Bruker Vertex 80v spectrometer in the Infrared & Raman for Interplanetary Spectroscopy

Laboratory (IRIS) at the Institut für Planetologie, University of Münster (Weber et al., 2025). Spectra were collected over areas limited by a knife-aperture with 25 × 25 µm to 40 × 40 µm, and a N_2-cooled MCT detector. Spots of pure glass were chosen based on the electron microscopy images and Raman spots, as well as the reflectance mode of the Hyperion microscope. A flat gold mirror was used as the background reference. For each measurement 512 spectra were averaged and collated over the spectral range of 2.7 to 16.7 µm (3900 to 600 cm^{-1}) at a spectral resolution of 4 cm^{-1}.

Characterization of experimental samples

We synthesized seven glass-bearing samples with compositions ranging from 0.5 to 97 wt.% SiO_2. In Figure S1 we show backscattered electron images of the samples with the areas in which we measured the spectral properties indicated in colored boxes. All samples show crystals, for example from unmolten or only partially molten starting material surrounding the beads. In addition, the low SiO_2 and high Al_2O_3 glasses (D6 and D5) show extensive quench crystallization. However, in all samples we identified sufficiently extensive areas that are chemically homogeneous and fully glassy without any quench crystals that allowed chemical and spectroscopic characterization of glasses with extremely high and extremely low SiO_2 contents. The electron microscopy images show no crystalline features in the indicated areas, where we measured the MIR reflectance and Raman spectra.

The compositions of the glass areas indicated in Figure S1 are shown in Table S1 for the major element oxides. We obtain systematically low totals around 97 wt.% for the glasses with very low SiO_2 contents. This is likely due to unusual matrix properties of these materials. Nevertheless, we do not normalize the concentrations and use the measured SiO_2 wt.% concentrations in the discussion. The compositional range spans from 97.6 wt.% SiO_2 to 0.5 wt.% SiO_2. The silica poor samples are in turn rich in CaO with up to 33 wt.% (D5) and Al_2O_3 with up to 58.5 wt.% (D6). The samples C1 and C3 are similar in SiO_2 content (64.1 and 59.4 wt.%, respectively), but vary substantially in Al_2O_3, FeO, MgO, and CaO (Table S1).

The glassy nature of the sample areas investigated is confirmed by Raman spectroscopy, with the spectra shown in Figure S2. All spectra are characteristic for purely glassy materials, without any sharp Raman lines indicative for crystalline phases. The spectrum of C2 shows the characteristic features of pure SiO_2 glass. The minor peaks at 494 cm^{-1} and 601 cm^{-1}, referred to as defect lines D_1 and D_2 and interpreted as 3- or 4-member SiO-ring structures, whereas the broad intensity maximum at 430 cm^{-1} corresponds to bond bending, the broad peak at 820 cm^{-1} to vibrations in the Si-O bond network, and the small and very broad band above 1000 cm^{-1} to the fully polymerized network of SiO_4^{4-} tetrahedra (Geissberger & Galeener, 1983; Little et al., 2008). The broad bands at 800 to 1200 cm^{-1} in the spectra C1, C3, D7, C8b, D6, and D5 are assigned to Si-O and Al-O stretching in the SiO_4 and AlO_4 tetrahedra with contributions from different degrees of polymerization, whereas bands at lower wavenumbers are related to inter-tetrahedral and rocking vibrations in the network (McMillan, 1984).

The mid-infrared spectra of the glasses, including the CF positions, are shown in Figure S3. The spectra show broad bands expected for glasses and similar to the Raman spectra. The reflectance maxima, referred to as main bands are also compositionally dependent. The maxima range from 8.2 µm for the silica glass C2 to >12.1 µm for the Si-poor glasses D7, C8b, D6, and D5. The observed band positions in the mid-infrared can be assigned to spectral units (Dalby & King, 2006). In the high SiO2 range the main bands at ~ 9.1 µm correspond to a fully polymerized network of tetrahedral units. In contrast, main band positions at ~ 12 µm are due to depolymerized SiO_4^{4-} units (v_1 symmetric Si–O stretch), observed in the low SiO_2 glasses. The spectra were processed using Python open-source packages (Hunter, 2007; Virtanen, 2020). The CF was identified by determining the position of lowest reflectance by finding the low-point in a given spectrum using the Pandas data analysis library (McKinney, 2010). The measured positions of the CFs are listed in Table S1.

References

Anand, M., Crawford, I. A., Balat-Pichelin, M., Abanades, S., van Westrenen, W., et al. (2012). A brief review of chemical and mineralogical resources on the Moon and likely initial in situ resource utilization (ISRU) applications. *Planetary and Space Science*, 74(1), 42–48. http://doi.org/https://doi.org/10.1016/j.pss.2012.08.012

Ashley, J. W., Robinson, M. S., Stopar, J. D., Glotch, T. D., Hawke, B. R., et al. (2016). The Lassell massif—A silicic lunar volcano. *Icarus*, 273, 248–261. http://doi.org/https://doi.org/10.1016/j.icarus.2015.12.036

Benkhoff, J., Murakami, G., Baumjohann, W., Besse, S., Bunce, E., et al. (2021). BepiColombo—Mission Overview and Science Goals. *Space Science Reviews*, 217(8), 90. http://doi.org/https://doi.org/10.1007/s11214-021-00861-4

Boschi, S., Wang, X.-L., Hui, H., Yin, Z., Guan, Y., et al. (2023). Compositional Variability of 2.0-Ga Lunar Basalts at the Chang'e-5 Landing Site. *Journal of Geophysical Research: Planets*, *128*(5), e2022JE007627. http://doi.org/https://doi.org/10.1029/2022JE007627

Boyce, J. M., Giguere, T. A., Hawke, B. R., Mouginis-Mark, P. J., Robinson, M. S., et al. (2017). Hansteen Mons: An LROC geological perspective. *Icarus*, 283, 254–267. http://doi.org/https://doi.org/10.1016/j.icarus.2016.08.013

Bunce, E. J., Martindale, A., Lindsay, S., Muinonen, K., Rothery, D. A., et al. (2020). The BepiColombo Mercury Imaging X-Ray Spectrometer: Science Goals, Instrument Performance and Operations. *Space Science Reviews*, 216(8), 126. http://doi.org/https://doi.org/10.1007/s11214-020-00750-2

Che, X., Nemchin, A., Liu, D., Long, T., Wang, C., et al. (2021). Age and composition of young basalts on the Moon, measured from samples returned by Chang'e-5. *Science*, 0(0), eabl7957. http://doi.org/https://doi.org/10.1126/science.abl7957

Chen, W., Qiu, D., Yan, J., & Yi, S. (2025). New insight into the composition of the lunar surface from SiO_2 map. *Frontiers in Astronomy and Space Sciences*, 12. http://doi.org/https://doi.org/10.3389/fspas.2025.1696995

Conel, J. E. (1969). Infrared emissivities of silicates: Experimental results and a cloudy atmosphere model of Spectral emission from condensed particulate mediums. *Journal of Geophysical Research (1896-1977)*, 74(6), 1614–1634. http://doi.org/https://doi.org/10.1029/JB074i006p01614

Cooper, B. L., Salisbury, J. W., Killen, R. M., & Potter, A. E. (2002). Midinfrared spectral features of rocks and their powders. *Journal of Geophysical Research: Planets*, 107(E4), 1-1-1–17. http://doi.org/https://doi.org/10.1029/2000JE001462

Dalby, K. N., & King, P. L. (2006). A new approach to determine and quantify structural units in silicate glasses using micro-reflectance Fourier-Transform infrared spectroscopy. *American Mineralogist*, 91(11–12), 1783–1793. http://doi.org/https://doi.org/10.2138/am.2006.2075

Donaldson Hanna, K. L., Wyatt, M. B., Thomas, I. R., Bowles, N. E., Greenhagen, T. B., et al. (2012). Thermal infrared emissivity measurements under a simulated lunar environment: Application to the Diviner Lunar Radiometer Experiment. *Journal of Geophysical Research: Planets*, 117(E00H05). http://doi.org/https://doi.org/10.1029/2011JE003862

Donaldson Hanna, K. L., Greenhagen, B. T., Patterson, W. R., Pieters, C. M., Mustard, J. F., et al. (2017). Effects of varying environmental conditions on emissivity spectra of bulk lunar soils: Application to Diviner thermal infrared observations of the Moon. *Icarus*, *283*, 326–342. http://doi.org/https://doi.org/10.1016/j.icarus.2016.05.034

Evans, L. G., Peplowski, P. N., Rhodes, E. A., Lawrence, D. J., McCoy, T. J., et al. (2012). Major-element abundances on the surface of Mercury: Results from the MESSENGER Gamma-Ray Spectrometer. *Journal of Geophysical Research: Planets*, 117(E12). http://doi.org/https://doi.org/10.1029/2012JE004178

First, E. C., Mishra, I., Gazel, E., Lewis, N. K., Letai, J., & Hanssen, L. (2025). Potential for observing geological diversity from mid-infrared spectra of rocky exoplanets. *Nature Astronomy*, 9(3), 370–379. http://doi.org/https://doi.org/10.1038/s41550-024-02412-7

Fraser, G. W., Carpenter, J. D., Rothery, D. A., Pearson, J. F., Martindale, A., et al. (2010). The mercury imaging X-ray spectrometer (MIXS) on bepicolombo. *Planetary and Space Science*, 58(1), 79–95. http://doi.org/https://doi.org/10.1016/j.pss.2009.05.004

Geissberger, A. E., & Galeener, F. L. (1983). Raman studies of vitreous SiO_2 versus fictive temperature. *Physical Review B*, 28(6), 3266–3271. http://doi.org/https://doi.org/10.1103/PhysRevB.28.3266

Glotch, T. D., Lucey, P. G., Bandfield, J. L., Greenhagen, B. T., Thomas, I. R., et al. (2010). Highly Silicic Compositions on the Moon. *Science*, 329(5998), 1510–1513. http://doi.org/https://doi.org/10.1126/science.1192148

Glotch, T. D., Jawin, E. R., Greenhagen, B. T., Cahill, J. T., Lawrence, D. J., et al. (2021). The Scientific Value of a Sustained Exploration Program at the Aristarchus Plateau. *The Planetary Science Journal*, 2(4), 136. http://doi.org/https://doi.org/10.3847/PSJ/abfec6

Greenhagen, B. T., Lucey, P. G., Wyatt, M. B., Glotch, T. D., Allen, C. C., et al. (2010). Global Silicate Mineralogy of the Moon from the Diviner Lunar Radiometer. *Science*, 329(5998), 1507–1509. http://doi.org/https://doi.org/10.1126/science.1192196

Gullikson, A. L., Hagerty, J. J., Reid, M. R., Rapp, J. F., & Draper, D. S. (2016). Silicic lunar volcanism: Testing the crustal melting model. *American Mineralogist*, 101(10), 2312–2321. http://doi.org/https://doi.org/10.2138/am-2016-5619

Hagerty, J. J., Lawrence, D. J., Hawke, B. R., Vaniman, D. T., Elphic, R. C., & Feldman, W. C. (2006). Refined thorium abundances for lunar red spots: Implications for evolved, nonmare volcanism on the Moon. *Journal of Geophysical Research: Planets*, 111(E6). http://doi.org/https://doi.org/10.1029/2005JE002592

Haupt, C. P., Stojic, A. N., Morlok, A., Weber, I., Klemme, S., et al. (2026). Mid-infrared spectroscopy of lunar high-Ti basalt analogues. *Journal of Geophysical Research: Planets*, 130, e2024JE008895. http://doi.org/https://doi.org/10.1029/2024JE008895

Hawke, B. R., Lawrence, D. J., Blewett, D. T., Lucey, P. G., Smith, G. A., et al. (2003). Hansteen Alpha: A volcanic construct in the lunar highlands. *Journal of Geophysical Research: Planets*, 108(E7). http://doi.org/https://doi.org/10.1029/2002JE002013

Heiken, G., Vaniman, D., & French, B. M. (Hrsg.) (1991). *Lunar Sourcebook: A User's Guide to The Moon*. Cambridge University Press.

Henderson, B. G., Jakosky, B. M. (1997). Near-surface thermal gradients and mid-IR emission spectra: A new model including scattering and application to real data. Journal of Geophysical Research, 102, 6567–6580. http://doi.org/https://doi.org/10.1029/96JE03781

Hiesinger, H., & Helbert, J. (2010). The Mercury Radiometer and Thermal Infrared Spectrometer (MERTIS) for the BepiColombo mission. *Planetary and Space Science*, 58(1), 144–165. http://doi.org/https://doi.org/10.1016/j.pss.2008.09.019

Hiesinger, H., Helbert, J., Alemanno, G., Bauch, K. E., D'Amore, M., et al. (2020). Studying the Composition and Mineralogy of the Hermean Surface with the Mercury Radiometer and Thermal Infrared Spectrometer (MERTIS) for the BepiColombo Mission: An Update. *Space Science Reviews*, 216(6), 110. http://doi.org/https://doi.org/10.1007/s11214-020-00732-4

Hunter, J.D. (2007) Matplotlib: A 2D Graphics Environment. *Computing in Science and Engineering*, 9, 90–95. http://doi.org/https://doi.org/10.1109/MCSE.2007.55

Iacovino, K., McCubbin, F. M., Vander Kaaden, K. E., Clark, J., Wittmann, A., et al. (2023). Carbon as a key driver of super-reduced explosive volcanism on Mercury: Evidence from graphite-melt smelting experiments. *Earth and Planetary Science Letters*, 602, 117908. http://doi.org/https://doi.org/10.1016/j.epsl.2022.117908

Keil, K., Kurat, G., Prinz, M., & Green, J. A. (1972). Lithic fragments, glasses and chondrules from Luna 16 fines. *Earth and Planetary Science Letters*, 13(2), 243–256. http://doi.org/https://doi.org/10.1016/0012-821X(72)90101-X

Korotev, R. L., & Gillis, J. J. (2001). A new look at the Apollo 11 regolith and KREEP. *Journal of Geophysical Research: Planets*, 106(E6), 12339–12353. http://doi.org/https://doi.org/10.1029/2000JE001336

Kumari, N., Glotch, T. D., Shirley, K. A., Greenhagen, B. T., Byron, B. D. (2024a) Effects of space weathering on the Christiansen feature position of lunar surface materials. *Icarus*, 115976. http://doi.org/https://doi.org/10.1016/j.icarus.2024.115976

Kumari, N., Glotch, T. D., Williams, J.-P., Sullivan, M. T., Li, S., Greenhagen, B. T., Waller, D., Powell, T., Elder, C. M., Byron, B. D., Shirley, K. A. (2024b) Extended silicic volcanism in the Gruithuisen region—Revisiting the composition and thermophysical properties of Gruithuisen Domes on the Moon. *The Planetary Science Journal*, 5, 132. http://doi.org/https://doi.org/10.3847PSJ/ad4352

Kumari N., Breitenfeld L. B., Shirley, K., Glotch, T. D. (2025) Characterizing extreme compositions on the Moon using thermal infrared spectroscopy. *Journal of Geophysical Research Planets*, 130, E2024JE008814. http://doi.org/https://doi.org/10.1029/E2024JE008814

Lee, R. J., King, P. L., & Ramsey, M. S. (2010). Spectral analysis of synthetic quartzofeldspathic glasses using laboratory thermal infrared spectroscopy. *Journal of Geophysical Research*, 115(B6). http://doi.org/https://doi.org/10.1029/2009JB006672

Li, C., Hu, H., Yang, M.-F., Pei, Z.-Y., Zhou, Q., et al. (2022). Characteristics of the lunar samples returned by the Chang'E-5 mission. *National Science Review*, 9(2), nwab188. http://doi.org/https://doi.org/10.1093/nsr/nwab188

Li, C., Hu, H., Yang, M.-F., Liu, J., Zhou, Q., et al. (2024). Nature of the lunar farside samples returned by the Chang'E-6 mission. *National Science Review*, nwae328. http://doi.org/https://doi.org/10.1093/nsr/nwae328

Little, D. J., Ams, M., Dekker, P., Marshall, G. D., Dawes, J. M., & Withford, M. J. (2008). Femtosecond laser modification of fused silica: The effect of writing polarization on Si-O ring structure. *Optics Express*, 16(24), 20029–20037. http://doi.org/https://doi.org/10.1364/OE.16.020029

Logan, L. M., Hunt, G. R. (1970). Emission spectra of particulate silicates under simulated lunar conditions. *Journal of Geophysical Research*, 75, 6539–6548.

Logan, L. M., Hunt, G. R., Salisbury, J. W., Balsamo, S. R. (1973). Compositional implications of Christiansen frequency maximums for infrared remote sensing applications. *Journal of Geophysical Research*, 78, 4983–5003. http://doi.org/https://doi.org/10.1029/JB078i023p04983

Lucey, P. G., Greenhagen, B. T., Song, E., Arnold, J. A., Lemelin, M., et al. (2017). Space weathering effects in Diviner Lunar Radiometer multispectral infrared measurements of the lunar Christiansen Feature: Characteristics and mitigation. *Icarus*, 283, 343–351. http://doi.org/https://doi.org/10.1016/j.icarus.2016.05.010

Lucey, P. G., Greenhagen, B., Donaldson Hanna, K., Bowles, N., Flom, A., & Paige, D. A. (2021). Christiansen feature map from the Lunar Reconnaissance Orbiter Diviner Lunar Radiometer experiment: Improved corrections and derived mineralogy. *Journal of Geophysical Research: Planets*, 126(6), e2020JE006777. http://doi.org/https://doi.org/10.1029/2020JE006777

Lunar Sample Compendium (2012). http://doi.org/https://curator.jsc.nasa.gov/lunar/lsc/

Ma, M., Li, B., Chen, S., Lu, T., Lu, P., et al. (2022). Global estimates of lunar surface chemistry derived from LRO diviner data. *Icarus*, 371, 114697. http://doi.org/https://doi.org/10.1016/j.icarus.2021.114697

Martindale, A., McKee, M. J., Bunce, E. J., Lindsay, S. T., Hall, G. P., et al. (2023). The BepiColombo Mercury Imaging X-Ray Spectrometer. In *Handbook of X-ray and Gamma-ray Astrophysics* (S. 1–55). Springer, Singapore. http://doi.org/https://doi.org/10.1007/978-981-16-4544-0_171-1

McCubbin, F. M., Vander Kaaden, K. E., Peplowski, P. N., Bell, A. S., Nittler, L. R., et al. (2017). A low O/Si ratio on the surface of Mercury: Evidence for silicon smelting? *Journal of Geophysical Research: Planets*, *122*(10), 2017JE005367. http://doi.org/https://doi.org/10.1002/2017JE005367

McKinney, W. (2010) Data Strucures for Statistical Computing in Python. *Proceedings of the 9th Python in Science Conference,* 56–61. http://doi.org/https://doi.org/10.25080/Majora-92bf1922-00a

McMillan, P. (1984). Structural studies of silicate glasses and melts – Applications and limitations of Raman spectroscopy. *American Mineralogist*, 69, 622–644.

Moriarty, D. P., Dygert, N., Valencia, S. N., Watkins, R. N., & Petro, N. E. (2021). The search for lunar mantle rocks exposed on the surface of the Moon. *Nature Communications*, 12(1), 4659. http://doi.org/https://doi.org/10.1038/s41467-021-24626-3

Morlok, A., Klemme, S., Weber, I., Stojic, A., Sohn, M., & Hiesinger, H. (2017). IR spectroscopy of synthetic glasses with Mercury surface composition: Analogs for remote sensing. *Icarus*, 296, 123–138. http://doi.org/https://doi.org/10.1016/j.icarus.2017.05.024

Morlok, A., Hamann, C., Martin, D., Weber, I., Joy, K. H., et al. (2020). Mid-infrared spectroscopy of laser-produced basalt melts for remote sensing application. *Icarus*, *335*, 113410. http://doi.org/https://doi.org/10.1016/j.icarus.2019.113410

Morlok, A., Renggli, C., Charlier, B., Reitze, M. P., Klemme, S., et al. (2021). Mid-infrared reflectance spectroscopy of synthetic glass analogs for mercury surface studies. *Icarus*, 361, 114363. http://doi.org/https://doi.org/10.1016/j.icarus.2021.114363

Morlok, A., Joy, K. H., Martin, D., Wogelius, R., Hiesinger, H. (2022). Laboratory IR spectroscopy of soils from Apollo 14, 15, and 16: Spectral parameters and maturity. *Planetary and Space Science*, 223, 105576. http://doi.org/https://doi.org/10.1016/j.pss.2022.105576

Nittler, L. R., Starr, R. D., Weider, S. Z., McCoy, T. J., Boynton, W. V., et al. (2011). The major-element composition of Mercury's surface from MESSENGER X-ray spectrometry. *Science*, 333(6051), 1847–1850. http://doi.org/https://doi.org/10.1126/science.1211567

Nittler, L. R., Chabot, N. L., Grove, T. L., & Peplowski, P. N. (2018). The Chemical Composition of Mercury. In S. C. Solomon, L. R. Nittler, & B. J. Anderson (Eds.), *Mercury, The View After MESSENGER* (1. Ed., S. 30–51). Cambridge University Press.

Nittler, L. R., Frank, E. A., Weider, S. Z., Crapster-Pregont, E., Vorburger, A., Starr, R. D., & Solomon, S. C. (2020). Global major-element maps of Mercury from four years of MESSENGER X-Ray Spectrometer observations. *Icarus*, 345, 113716. http://doi.org/https://doi.org/10.1016/j.icarus.2020.113716

Pisello, A., Ferrari, M., De Angelis, S., Vetere, F.P., Porreca, M., Stefani, S., Perugini, D. (2022) Reflectance of silicate glasses in the mid-infrared region (MIR): Implications for planetary research. *Icarus*, 388, 115222. http://doi.org/https://doi.org/10.1016/j.icarus.2022.115222

Prettyman, T. H., Hagerty, J. J., Elphic, R. C., Feldman, W. C., Lawrence, D. J., et al. (2006). Elemental composition of the lunar surface: Analysis of gamma ray spectroscopy data from Lunar Prospector. *Journal of Geophysical Research: Planets*, 111(E12). http://doi.org/https://doi.org/10.1029/2005JE002656

Qiu, D., Ye, M., Yan, J., Zheng, C., Xiao, Z., et al. (2022). New view of the lunar silicic volcanism in the Mons Hansteen: Formation and origins. *Journal of Geophysical Research: Planets*, 127(8), e2022JE007289. http://doi.org/https://doi.org/10.1029/2022JE007289

Qiu, D., Sasaki, S., Yan, J., Ye, M., Deng, Q., et al. (2023). Buried silicic volcanoes discovered in the Gruithuisen region on the Moon. *Geophysical Research Letters*, 50(11), e2023GL103336. http://doi.org/https://doi.org/10.1029/2023GL103336

Qiu, D., Yan, J., & Huang, J. (2025). Explosive volcanic eruption at Lassell Massif: Implications for lunar silicic volcanism. *Icarus*, 441, 116730. http://doi.org/https://doi.org/10.1016/j.icarus.2025.116730

Ravi, S., Till, C. B., & Robinson, M. S. (2025). On the origin of silicic magmas on the Moon. *The Planetary Science Journal*, 6(9), 223. http://doi.org/https://doi.org/10.3847/PSJ/adf7a4

Rutherford, M. J., Hess, P. C., Ryerson, F. J., Campbell, H. W., & Dick, P. A. (1976). The chemistry, origin and petrogenetic implications of lunar granite and monzonite. *Proc. Lunar Planet. Sci.*, 7, 1723–1740.

Salisbury, J. W., & Walter, L. S. (1989). Thermal infrared (2.5–13.5 µm) spectroscopic remote sensing of igneous rock types on particulate planetary surfaces. *Journal of Geophysical Research: Solid Earth*, 94(B7), 9192–9202. http://doi.org/https://doi.org/10.1029/JB094iB07p09192

Seddio, S. M., Jolliff, B. L., Korotev, R. L., & Zeigler, R. A. (2013). Petrology and geochemistry of lunar granite 12032,366-19 and implications for lunar granite petrogenesis. *American Mineralogist*, 98(10), 1697–1713. http://doi.org/https://doi.org/10.2138/am.2013.4330

Seddio, S. M., Jolliff, B. L., Korotev, R. L., & Carpenter, P. K. (2014). Thorite in an Apollo 12 granite fragment and age determination using the electron microprobe. *Geochimica et Cosmochimica Acta*, 135, 307–320. http://doi.org/https://doi.org/10.1016/j.gca.2014.03.020

Salisbury, J. W., Basu, A., Fischer, E. M. (1997). Thermal infrared spectra of lunar soils. *Icarus*, 130, 125–139. http://doi.org/https://doi.org/10.1006/icar.1997.5809

Shirley, K. A., Glotch, T. D. (2019). Particle Size Effects on Mid-Infrared Spectra of Lunar Analog Minerals in a Simulated Lunar Environment. *Journal of Geophysical Research: Planets*, 124, 970-988. http://doi.org/https://doi.org/10.1029/2018JE005533

Sprague, A. (2000). Mid-Infrared (8.1–12.5 µm) Imaging of Mercury. *Icarus*, 147(2), 421–432. http://doi.org/https://doi.org/10.1006/icar.2000.6447

Taylor, G. J., Warner, R. D., Wentworth, S., Keil, K., & Usman, S. (1978). Luna 24 lithologies: Petrochemical relationships among lithic fragments, mineral fragments, and glasses. *Mare Crisium: The view from Luna 24, Proceedings*, 303–320.

Valencia, S. N., Korotev, R. L., & Jolliff, B. L. (2024). Compositional analysis of Apollo 12 Granitic Breccia 12013: Insights into protoliths and formation. *Geochimica et Cosmochimica Acta*, 367, 189–212. http://doi.org/https://doi.org/10.1016/j.gca.2023.12.034

Vander Kaaden, K. E., & McCubbin, F. M. (2016). The origin of boninites on Mercury: An experimental study of the northern volcanic plains lavas. *Geochimica et Cosmochimica Acta*, 173, 246–263. http://doi.org/https://doi.org/10.1016/j.gca.2015.10.016

Vander Kaaden, K. E., McCubbin, F. M., Nittler, L. R., Peplowski, P. N., Weider, S. Z., et al. (2017). Geochemistry, mineralogy, and petrology of boninitic and komatiitic rocks on the mercurian surface: Insights into the mercurian mantle. *Icarus*, 285, 155–168. http://doi.org/https://doi.org/10.1016/j.icarus.2016.11.041

Virtanen, P. (2020) SciPy 1.0: Fundamental Algorithms for Scientific Computing in Python. *Nature Methods*, 17, 261–272. http://doi.org/https://doi.org/10.1038/s41592-019-0686-2

Wang, B.-W., Zhang, Q. W. L., Chen, Y., Zhao, W., Liu, Y., et al. (2024). Returned samples indicate volcanism on the Moon 120 million years ago. *Science*, 385(6713), 1077–1080. http://doi.org/https://doi.org/10.1126/science.adk6635

Wang, Z., Li, Y., Li, J., Zong, K., She, Z., et al. (2025). Chemical compositions of Chang'e-6 lunar soil and substantial addition of noritic crust ejecta from Apollo basin. *Geology*, 53(7), 557–561. http://doi.org/https://doi.org/10.1130/G53086.1

Warren, P. H., Taylor, G. J., Keil, K., Shirley, D. N., & Wasson, J. T. (1983). Petrology and chemistry of two "large" granite clasts from the moon. *Earth and Planetary Science Letters*, 64(2), 175–185. http://doi.org/https://doi.org/10.1016/0012-821X(83)90202-9

Weber, I., Stojic, A. N., Morlok, A., Reitze, M. P., Markus, K., Hiesinger, H., Pavlov, S. G., Wirth, R., Schreiber, A., Sohn, M., Hübers, H.-W., Helbert, J. (2020). Space weathering by simulated micrometeorite bombardment on natural olivine and pyroxene: A coordinated IR and TEM study. *Earth and Planetary Science Letters*, 530, 115884. http://doi.org/https://doi.org/10.1016/j.epsl.2019.115884

Weber, I., Reitze, M. P., Morlok, A., Stojic, A. N., Hiesinger, H., et al. (2023). Mid-IR spectral properties of different surfaces of silicate mixtures before and after excimer laser irradiation. *Icarus*, 404, 115683. http://doi.org/https://doi.org/10.1016/j.icarus.2023.115683

Weber, I., Reitze, M. P., Heyer, T., Morlok, A., Grund, T., & Hiesinger, H. (2026). The IRIS reflectance IR database for space missions. *Advances in Space Research*, 77(3), 3934–3946. http://doi.org/https://doi.org/10.1016/j.asr.2025.12.048

Weider, S. Z., Nittler, L. R., Starr, R. D., McCoy, T. J., Stockstill-Cahill, K. R., et al. (2012). Chemical heterogeneity on Mercury's surface revealed by the MESSENGER X-Ray Spectrometer: Chemical heterogeneity on Mercury. *Journal of Geophysical Research: Planets*, 117(E12). http://doi.org/https://doi.org/10.1029/2012JE004153

Weider, S. Z., Nittler, L. R., Starr, R. D., McCoy, T. J., & Solomon, S. C. (2014). Variations in the abundance of iron on Mercury's surface from MESSENGER X-Ray Spectrometer observations. *Icarus*, 235, 170–186. http://doi.org/https://doi.org/10.1016/j.icarus.2014.03.002

Weider, S. Z., Nittler, L. R., Starr, R. D., Crapster-Pregont, E. J., Peplowski, P. N., et al. (2015). Evidence for geochemical terranes on Mercury: Global mapping of major elements with MESSENGER's X-Ray Spectrometer. *Earth and Planetary Science Letters*, 416, 109–120. http://doi.org/https://doi.org/10.1016/j.epsl.2015.01.023

Weitz, C. M., Head, J. W., & Pieters, C. M. (1998). Lunar regional dark mantle deposits: Geologic, multispectral, and modeling studies. *Journal of Geophysical Research: Planets*, 103(E10), 22725–22759. http://doi.org/https://doi.org/10.1029/98JE02027

Wilbur, W. Z., Barnes, J. J., Eckley, S. A., Erickson, T., Zeigler, R. A., Domanik, K. (2025) Evaluating the crystallization and eruptive histories of low-titanium basalts with 2D and 3D studies. *Geochimica et at Cosmochimica Acta*, 389, 110–124. http://doi.org/https://doi.org/10.1016/j.gca.2024.10.018

Wieczorek, M. A., Neumann, G. A., Nimmo, F., Kiefer, W. S., Taylor, G. J., et al. (2013). The crust of the Moon as seen by GRAIL. *Science*, 339(6120), 671–675. http://doi.org/https://doi.org/10.1126/science.1231530

Yang, C., Zhang, X., Bruzzone, L., Liu, B., Liu, D., et al. (2023). Comprehensive mapping of lunar surface chemistry by adding Chang'e-5 samples with deep learning. *Nature Communications*, 14(1), 7554. http://doi.org/https://doi.org/10.1038/s41467-023-43358-0

Zhao, R., Shen, L., Xiao, D., Chang, C., Huang, Y., et al. (2023) Diverse glasses revealed from Chang'E-5 lunar regolith. *National Science Review*, 10, nwad079. http://doi.org/https://doi.org/10.1093/nsr/nwad079

Zong, K., Wang, Z., Li, J., He, Q., Li, Y., et al. (2022). Bulk compositions of the Chang'E-5 lunar soil: Insights into chemical homogeneity, exotic addition, and origin of landing site basalts. *Geochimica et Cosmochimica Acta*, 335, 284–296. http://doi.org/https://doi.org/10.1016/j.gca.2022.06.037